minerals

MDPI

Article

Micro-Topographic Controls on Rare Earth Element Accumulation and Fractionation in Weathering Profiles: Case Study of Ion-Adsorption Rare Earth Element Deposit in Hedi, Zhejiang Province, China

Wenlin Guo [1,2], Zhi Zhao [3,*], Chengshan Wang [1], Denghong Wang [3], Xiaorong Chen [4], Xiaoliang Dang [4], Wei Zhang [4] and Chenhui Zhao [3]

[1] School of Earth Sciences and Resources, China University of Geosciences, Beijing 100083, China; gwenlin@mail.cgs.gov.cn (W.G.); chshwang@cugb.edu.cn (C.W.)
[2] China Geological Survey, Beijing 100037, China
[3] MNR Key Laboratory of Metallogeny and Mineral Assessment, Institute of Mineral Resources, Chinese Academy of Geological Sciences, Beijing 100037, China; wangdenghong@mail.cgs.gov.cn (D.W.); geochenhui@163.com (C.Z.)
[4] The Seventh Geological Brigade of Zhejiang Province, Lishui 323000, China; cxr101112@163.com (X.C.); dangxiaoliang@126.com (X.D.); zweideyx@outlook.com (W.Z.)
* Correspondence: zhaozhi@mail.cgs.gov.cn; Tel.: +86-13661049730

Abstract: Ion-adsorption rare earth element (REE) deposits are a major source of REEs and are found mainly in China. The formation of such deposits is affected by a combination of endogenic and exogenic factors. This study investigated the effect of micro-topography on the REE distribution in four weathering profiles at different topographic sites on a knoll in Hedi, Zhejiang Province, China. The weathering profile and REE accumulation are both most developed at mid-slope positions of the knoll. The intensity of chemical weathering decreases in the order of mid-slope > base > summit. As weathering progressed, REE enrichment initially increased but later decreased, with a progressive increase in light/heavy REE fractionation. REE fractionation is more pronounced on the north-facing slope than on the south-facing slope. Weathering degrees and clay mineral characteristics are key factors influencing the varying REE distributions on the knoll. Water leaching and the evolution of clay minerals towards higher maturity reduce REE adsorption capacity. Clay minerals also play a significant role in REE fractionation; the abundance of these minerals and the presence of illite enable the retention of more HREEs with minimal desorption. Taking into account water content, it is inferred that hydrological conditions, modulated by the micro-topography, strongly affect the depth and extent of REE accumulation, as well as fractionation.

Keywords: ion-adsorption REE deposit; micro-topography; REE accumulation and fractionation; chemical weathering; Hedi granite

Citation: Guo, W.; Zhao, Z.; Wang, C.; Wang, D.; Chen, X.; Dang, X.; Zhang, W.; Zhao, C. Micro-Topographic Controls on Rare Earth Element Accumulation and Fractionation in Weathering Profiles: Case Study of Ion-Adsorption Rare Earth Element Deposit in Hedi, Zhejiang Province, China. *Minerals* **2024**, *14*, 1178. https://doi.org/10.3390/min14111178

Academic Editor: Maria Economou-Eliopoulos

Received: 26 September 2024
Revised: 4 November 2024
Accepted: 7 November 2024
Published: 20 November 2024

1. Introduction

Rare earth elements (REEs) have unique optical, electromagnetic, and catalytic properties. They are widely used in agricultural, metallurgical, glass ceramic, and petroleum industries, as well as advanced technologies including clean energy, aerospace, and healthcare [1,2]. Amongst the various types of REE deposits, ion-adsorption deposits have significant economic value due to their high contents of heavy REEs (HREEs), relative ease of extraction, and lower levels of radioactive elements [3]. Recently, research on ion-adsorption REE deposits has increased globally, leading to substantial advances in our understanding of their mineralization processes and mineral exploration techniques [4].

Ion-adsorption REE deposits are found mainly in the southern Chinese provinces of Jiangxi, Guangxi (Zhuang Autonomous Region), Guangdong, and Fujian, which account

for the majority of global HREE production. These deposits have also been identified in some Southeast Asian countries, as well as in Madagascar, Brazil, and the USA [4,5]. The formation of ion-adsorption REE deposits is affected by endogenic factors (e.g., the parent rock type, composition of primary REE minerals, and physical structure) and exogenic factors (e.g., climate, topography, and biological activity) [6–8]. Prolonged weathering of bedrock leads to the development of a thick regolith, where ionic REEs accumulate by adsorption onto secondary clay minerals or Fe–Mn oxyhydroxides [9–11]. Various factors, such as water, temperature, pH, and organic matter, collectively affect the geochemical behavior of REEs within these deposits, which controls REE activation, migration, accumulation, and fractionation [4,6,12,13]. The prevalence of granitoids in southern China [6,13,14], combined with its warm, humid, subtropical climate and hilly terrain, creates favorable conditions for the formation of ion-adsorption REE deposits.

In southern China, ion-adsorption REE deposits are found primarily in low-altitude (100–300 m), gently sloping, and well-drained hilly regions [12,15,16]. However, such deposits have also been discovered at higher altitudes and latitudes in southern China, such as the Hedi area in Zhejiang Province. Topography has a key role in the mineralization of, and exploration for, ion-adsorption REE deposits [17]. Factors such as the altitude, slope gradient, relief, and surface dissection affect the spatial distribution of REEs, ore body thickness, and ore grade [5,16]. However, the relationship between REE enrichment and micro-topographic features varies amongst different deposits [12,18–20]. For example, the Cenxi deposit in Guangxi Province and Menghai deposit in Yunnan Province have a greater deposit thickness and higher ore grades at mid-slope positions [21], whereas the Chongzuo Jiangzhou deposit in Guangxi Province has thicker deposits and higher ore grades at hilltops [22]. As such, further research is needed to elucidate how topographic factors affect REE accumulation and fractionation.

In this study, we selected four distinct topographic locations on a specific knoll within the Hedi ion-adsorption REE deposit. We compared the mineralogical and geochemical characteristics of weathering profiles at these locations, with a particular focus on REE patterns, to examine the effect of micro-topography on REE accumulation and fractionation during weathering.

2. Hedi Granite

The Hedi Granite is located in Qingyuan County, Lishui City, in southwestern Zhejiang Province (Figure 1). It has an outcrop area of ~67 km^2 and is characterized by a NE–SW-trending, stock-like intrusion that was emplaced into Late Jurassic volcanic rocks. The lithology consists of light gray to pink, biotite monzogranitic porphyry and hornblende–biotite monzogranitic porphyry [18,23]. The pluton yields a zircon U–Pb age of 135 Ma and a total REE content of 264–311 ppm [23].

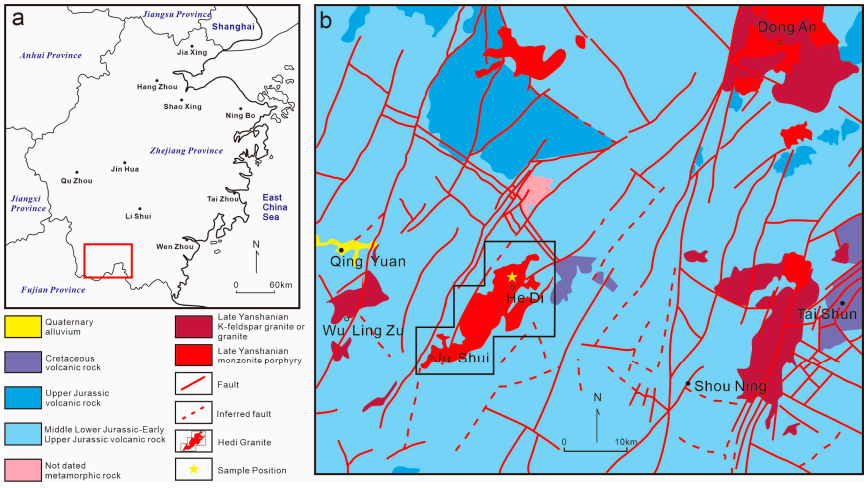

Figure 1. (**a**) Sketch location map and (**b**) geological map of Hedi Granite.

3. Weathering Profile

Qingyuan County is located on the highest and largest plateau in Zhejiang Province, with elevations of 500–1400 m and an average of ~980 m. The region falls within the Central Asian subtropical monsoonal climate zone, which is characterized by an average annual temperature of 18 °C, relative humidity of 77%, and annual precipitation of 1747 mm. The Hedi Granite has undergone intense weathering, leading to the formation of a regolith that overlies the bedrock. The regolith is typically 8–10 m thick, but locally exceeds 20 m. The weathering profile has a layered structure that can be divided into several horizons as follows.

Humus horizon (A_1 horizon): This layer extends from the surface to a depth of 0–0.2 m and is characterized by a dark brown coloration, and abundant plant roots, and consists primarily of clay minerals and quartz.

Clay horizon (A_2 horizon): This horizon occurs at a 0.2–1.5 m depth and exhibits red–brown to brick red colors and contains few plant roots. It is more compact and less permeable than the A_1 horizon, consisting mainly of clay minerals and minor amounts of alkali feldspar weathering residues, quartz, biotite (or muscovite) fragments, and black Fe–Mn oxyhydroxides.

Fully weathered horizon (B horizon): This horizon occurs at a 1.5–8.0 m depth and has a red–brown to yellow–brown mottled appearance with a soil-like texture. The structure is loose and highly permeable. Plagioclase is entirely weathered into clay minerals, alkali feldspar is minimally weathered, biotite is transformed into flaky muscovite, and quartz particles are residual grains of the bedrock. Locally, black Fe–Mn oxyhydroxides are present.

Semi-weathered horizon (C horizon): This horizon occurs at depths of 7–8 m and ranges from gray–red to light gray–purple in color. Drillcores often fail to fully penetrate this horizon owing to strong hardness. It is characterized by well-developed fractures and weaker weathering as compared with the B horizon, and has a good permeability. Alkali feldspar only exhibits slight surface weathering into clay minerals, whereas plagioclase is largely weathered into clay minerals. This horizon contains spheroidal residues of unweathered bedrock, with individual fragments of 10–50 cm in diameter, and locally >100 cm.

Parent rock (D horizon): At a >8 m depth, this horizon consists of light pink biotite monzonitic granite with a porphyritic texture and blocky structure. Phenocrysts comprise 25–35 vol. % of the rock, including plagioclase, alkali feldspar, quartz, biotite, and hornblende. The matrix is light pink in color and consists of alkali feldspar, plagioclase, quartz, biotite, and accessory chlorite, magnetite, apatite, and zircon.

4. Materials and Methods

4.1. Sampling

The study area is situated in a hilly region with elevations of 900–1300 m, characterized by gently undulating terrain. The elevation difference between the summit and base of the knoll is 50 m, with the knoll extending 700 m N–S and 250 m E–W, and slope gradients ranging from 0° to 15°. Four profiles were sampled along the hillslope, including the summit, the south (S)-facing mid-slope, the north (N)-facing mid-slope, and the base (Figure 2). These profiles were drilled to depths of 8.1, 7.9, 8.5, and 7.9 m, respectively. The stratigraphic characteristics of each profile are shown in Figure 3. The total thickness of the A_2 and B horizons is generally thinner at the summit as compared with the mid-slope and base. In detail, the B horizon is thickest on the N-facing mid-slope, while the A_2 horizon is thickest on the S-facing mid-slope. A total of 32 regolith samples and 1 sample of parent rock were collected, with sampling intervals in each borehole of ~1 m. Each sample was mixed and sealed in polyethylene bags, with a 3 kg aliquot selected for the analysis. The parent rock sample (Figure 4) was obtained from a deep hard-rock borehole drilled by the Seventh Geological Brigade of Zhejiang Province, Lishui, China. Given that the A_1 horizon is generally thin, has experienced complex pedogenic processes, and has low REE contents, sampling commenced at a depth of 1 m.

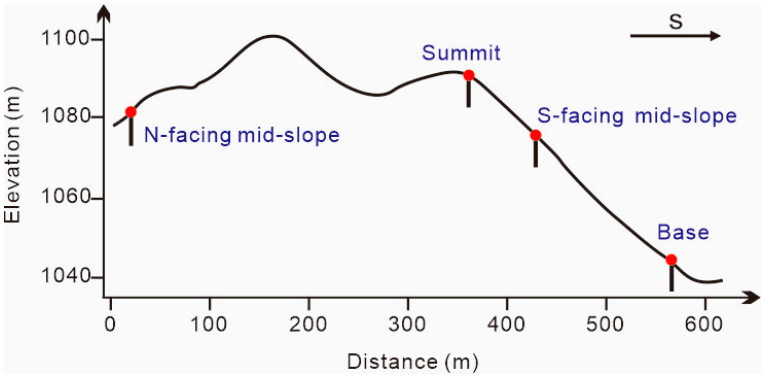

Figure 2. A sketch map showing the locations of sampling profiles on the knoll.

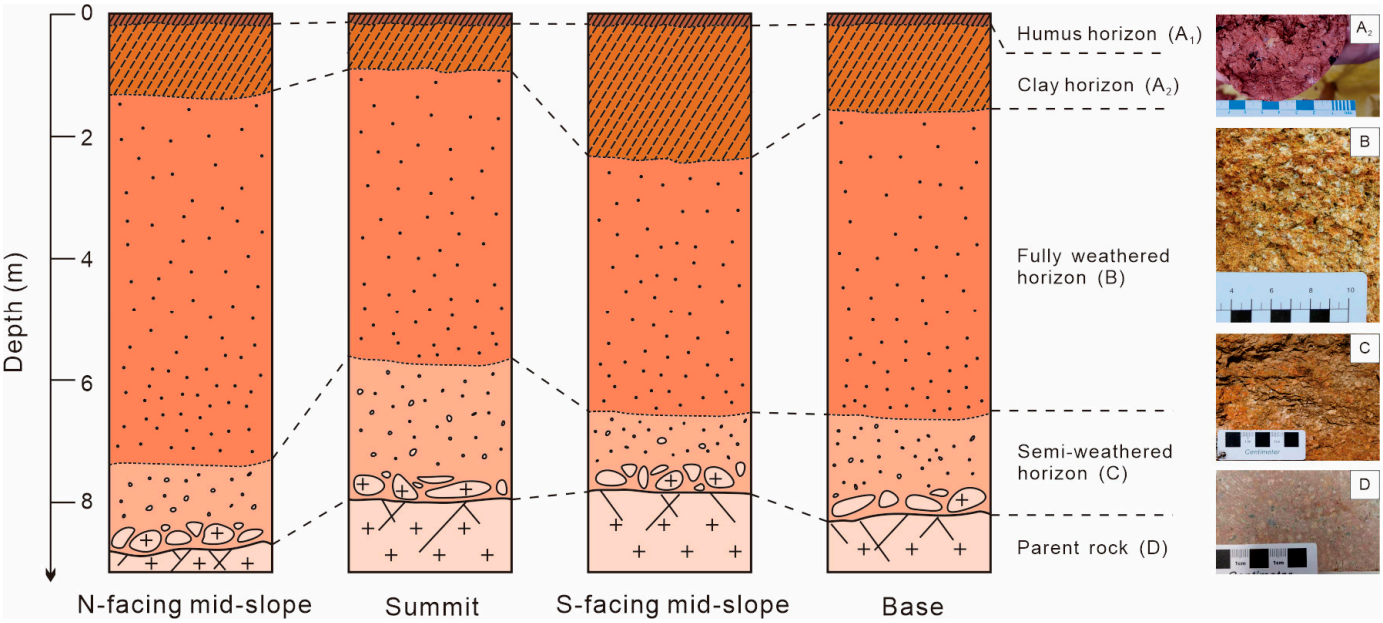

Figure 3. Sketches of the layered weathering profiles at the summit, S-facing mid-slope, N-facing mid-slope, and base of the knoll.

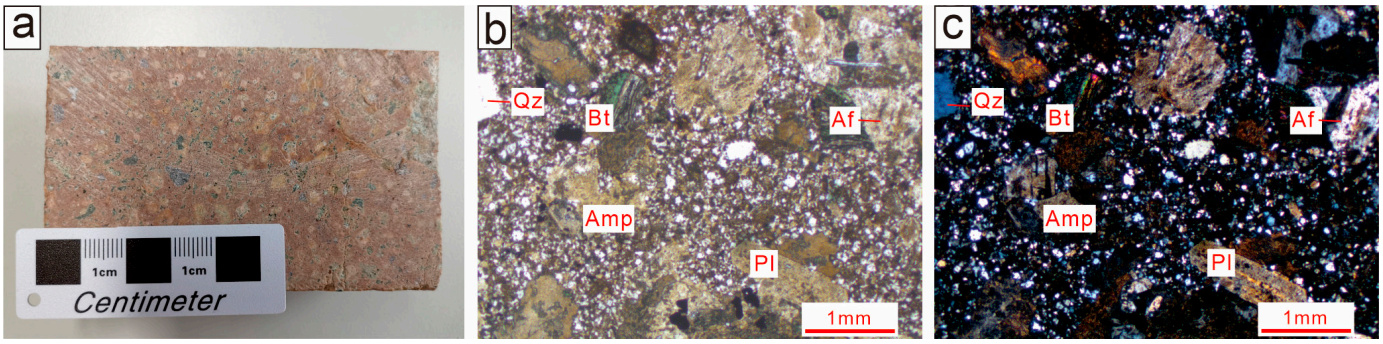

Figure 4. (**a**) Photograph, (**b**) photomicrograph under plane-polarized light, and (**c**) corresponding cross-polarized light photomicrograph of bedrock. Qz—Quartz; Bt—Biotite; Af—Alkali feldspar; Amp—Amphibole; Pl—Plagioclase.

4.2. Analytical Methods

After sample collection and packaging, the samples were weighed and transported to a laboratory, where they were dried in an oven at 105 °C for 24 h and then weighed again before grounding to 200 mesh for a further analysis. The water content can be calculated

from the difference in mass. The parent rock sample was made into standard thin sections for petrological observations. Major elements were analyzed by X-ray fluorescence (XRF) spectrometry with an ARL ADVANT XP instrument (Thermo Fisher Scientific, Beijing, China) Weighed aliquots of 0.4 g of sample powder were mixed with 4 g of a flux consisting of lithium tetraborate, lithium metaborate, and lithium fluoride, and then fused into glass beads using a fusion method. The analytical precision of the major element data was better than ±1%. The determination of FeO was carried out using the sulfuric acid–hydrofluoric acid dissolution–potassium dichromate titration method. Trace elements were measured by inductively coupled plasma–mass spectrometry (ICP–MS) with an ICP–MS 7500ce instrument (Agilent Technologies, Bejing, China). For a trace element analysis, rock powders were acid-digested in a high-pressure vessel to obtain solutions for the analysis, with relative errors of less than 5%. Whole-rock geochemical analyses were conducted at the Key Laboratory of Orogenic Belts and Crustal Evolution, Peking University, Beijing, China. A mineralogical analysis was performed with a Bruker D8 Advance X-ray diffractometer (XRD) at the Institute of Mineral Resources, Chinese Academy of Geological Sciences, Beijing, China. Sample powders were carefully packed into glass sample holders to test, and the resulting diffractograms were evaluated, and the proportions of various minerals were determined through Rietveld refinement with JADE 6.5 software.

5. Results

5.1. Water Content

The water contents of the weathering profile samples are presented in Table 1, with their variations with depth illustrated in Figure 5. Notably, the upper portion of the base profile exhibits higher water content compared to the other profiles. At the summit, there is a progressive decrease in water content with depth. In contrast, at the mid-slope, water gradually infiltrates the soil, resulting in an increase in water content downward, where it accumulates between the B and C horizons. At the base, fluctuations in water content diminish as one progresses deeper into the profile.

Table 1. Water contents for the studied weathering profiles.

Profile Location	Sample Number	Depth (m)	Water Content (%)	Profile Location	Sample Number	Depth (m)	Water Content (%)
Summit	HD120101	0.6	21.1	**N-facing mid-slope**	HD112906	0.4	21.2
	HD120102	1.8	22.9		HD112907	1.5	20.8
	HD120103	2.9	22.7		HD112908	2.9	22.1
	HD120104	3.9	21.7		HD112909	4.3	22.6
	HD120105	4.9	22.2		HD112910	5.4	22.7
	HD120106	5.9	21.3		HD112911	6.5	23.1
	HD120107	6.9	20.9		HD113002	7.6	24.2
	HD120108	7.9	21.0		HD113003	8.5	21.9
S-facing mid-slope	HD113021	0.7	22.4	**Base**	HD113013	0.6	24.1
	HD113022	1.9	20.5		HD113014	1.8	22.2
	HD113023	2.9	21.4		HD113015	2.8	22.5
	HD113024	3.9	22.0		HD113016	3.9	22.8
	HD113025	4.9	NA		HD113017	4.9	21.1
	HD113026	5.9	22.9		HD113018	5.9	21.9
	HD113027	6.9	22.1		HD113019	7.0	22.5
	HD113028	7.9	21.6		HD113020	8.1	19.7

NA—This sample was not analyzed.

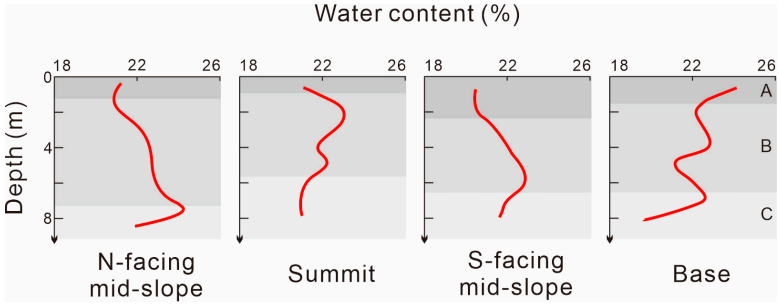

Figure 5. Plots of water contents versus depth for the studied weathering profiles. A—humus and clay horizon; B—fully weathered horizon; C—semi-weathered horizon.

5.2. Mineral Compositions

The whole-rock mineral contents of the samples are summarized in Table 2, and their variations with depth are shown in Figure 6. The XRD analysis revealed that the regolith consists primarily of quartz, alkali feldspar, and clay minerals. Quartz contents range from 53 to 88 wt. %, while alkali feldspar contents vary between 3 and 31 wt. %. The quartz content exhibits fluctuating variation along the vertical profile. The alkali feldspar content generally increases with depth, with higher contents at the summit and base, and lower contents at the mid-slope profiles. Clay mineral contents range from 4 to 47 wt. %, with higher contents at the mid-slope and lower contents at the summit and base. The identified clay minerals are predominantly kaolinite (halloysite), with minor amounts of illite and trace amounts of gibbsite. Illite was not detected at either the summit or the base, and gibbsite was absent at the summit. The variation in clay minerals along the vertical profile exhibits an inverse correlation with that of alkali feldspar.

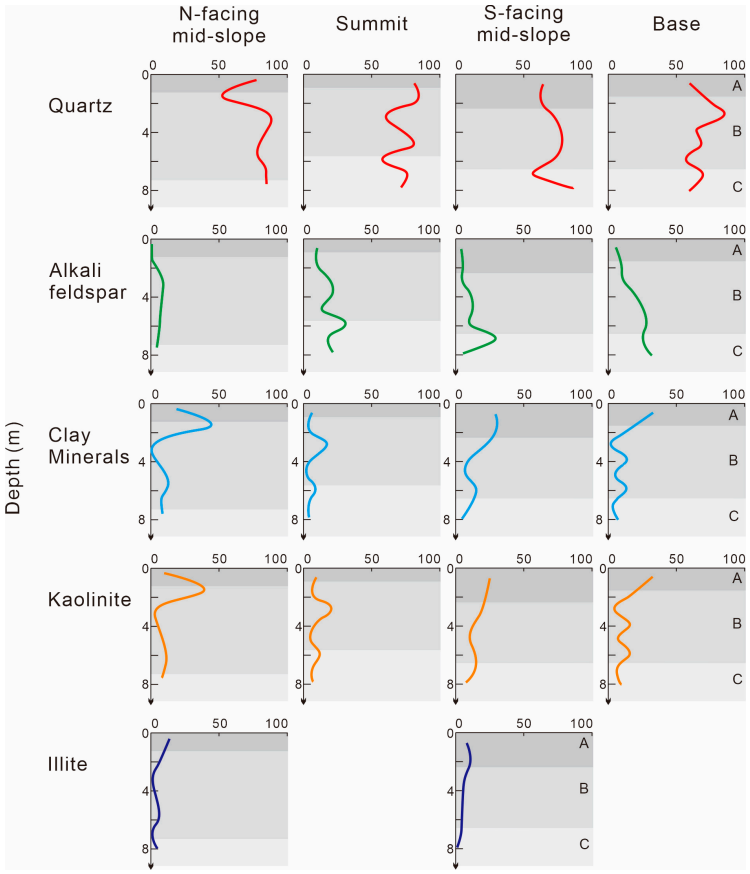

Figure 6. Plots of minerals' contents versus depth for the studied weathering profiles. A—humus and clay horizon; B—fully weathered horizon; C—semi-weathered horizon.

Table 2. Mineral concentrations measured by XRD for the studied weathering profiles.

Profile Position	Sample Number	Depth (m)	Qz (%)	Af (%)	Kl (%)	Ill (%)	Gib (%)	Clay (%)	Profile Position	Sample Number	Depth (m)	Qz (%)	Af (%)	Kl (%)	Ill (%)	Gib (%)	Clay (%)
Summit	HD120101	0.6	81.8	9.3	8.9	BD	BD	8.9	N-facing mid-slope	HD112906	0.4	78.5	BD	8.3	12.9	0.4	21.6
	HD120102	1.8	84.5	9.2	6.3			6.3		HD112907	1.5	52.6	BD	39.1	8.0	0.3	47.4
	HD120103	2.9	60.9	19.1	20.1			20.1		HD112908	2.9	51.0	8.0	2.9	0.6	0.2	3.7
	HD120104	3.9	70.9	21.4	7.7			7.7		HD112909	4.3	NA					
	HD120105	4.9	81.8	13.7	4.4			4.4		HD112910	5.4	78.6	5.9	9.4	5.5	0.7	15.6
	HD120106	5.9	57.2	31.2	11.7			11.7		HD112911	6.5	84.3	5.1	10.6	BD	BD	10.6
	HD120107	6.9	76.3	17.3	6.4			6.4		HD113002	7.6	85.5	3.5	7.5	3.4	BD	10.9
	HD120108	7.9	72.0	21.5	6.5			6.5		HD113003	8.5	NA					
S-facing mid-slope	HD113021	0.7	64.4	3.4	24.6	7.7	BD	32.3	Base	HD113013	0.6	60.0	5.1	32.0	BD	2.9	34.9
	HD113022	1.9	62.7	4.8	22.1	10.4	0.1	32.6		HD113014	1.8	73.0	9.1	17.7		0.3	18.0
	HD113023	2.9	71.4	3.9	18.8	5.9	BD	24.7		HD113015	2.8	86.2	10.2	3.4		0.2	3.6
	HD113024	3.9	77.2	10.4	12.4	BD	BD	12.4		HD113016	3.9	65.7	19.1	15.2		BD	15.2
	HD113025	4.9	78.7	11.9	9.4	BD	BD	9.4		HD113017	4.9	68.7	25.0	6.3		BD	6.3
	HD113026	5.9	72.9	9.4	13.7	4.0	BD	17.7		HD113018	5.9	57.1	27.6	15.2		BD	15.2
	HD113027	6.9	56.6	28.9	14.4	BD	BD	14.4		HD113019	7.0	70.0	24.6	5.4		BD	5.4
	HD113028	7.9	87.2	5.2	7.6	BD	BD	7.6		HD113020	8.1	59.8	31.3	8.8		0.1	8.9

Qz—Quartz; Af—Alkali feldspar; Kl—Kaolinite; Ill—Illite; Gib—Gibbsite; BD—This mineral content is below the detection; NA—This sample was not analyzed.

5.3. Major Element Compositions

The whole-rock major element data are presented in Table 3. To characterize the loss or gain of major elements, the dimensionless mass transfer coefficient τ_j of j element was calculated. $\tau_j = (C_{j,r}/C_{i,r})/(C_{j,p}/C_{i,p}) - 1$, with i as the inert reference element, C representing element concentration, and r and p indicating regolith and parent rock, respectively [24–26]. Considering that weathering causes volume changes, the volumetric strain values of the inert elements Ti, Zr, Nb, and Hf were calculated based on the density of the weathering profile [26]. Ti is the most suitable element according to the results. The τ_j values are plotted versus depth in Figure 7. In the profiles, with the exception of Al, Fe, and Mn, all other major elements exhibit varying degrees of depletion. Mobile elements such as Na, Ca, P, and Mg are notably leached, while Si and K are slightly leached and depleted. The extent of depletion is less pronounced at the summit and more significant at the mid-slope. Relatively stable Al exhibits significant enrichment at the summit. Manganese is progressively enriched with increasing depth in the profiles.

Table 3. Major element concentrations measured by XRF for the studied weathering profiles and parent rock.

Profile Position	Sample Number	Depth (m)	Major Elements' Content (%)												CIA (%)
			SiO_2	Al_2O_3	CaO	FeO	TFe_2O_3	K_2O	MgO	MnO	Na_2O	P_2O_5	TiO_2	LOI	
Summit	HD120101	0.6	59.31	26.01	0.02	0.14	3.07	3.62	0.16	0.07	0.20	0.02	0.42	7.03	85.84
	HD120102	1.8	60.48	24.58	0.02	0.13	3.03	4.60	0.15	0.09	0.08	0.02	0.41	6.45	82.68
	HD120103	2.9	58.72	26.56	0.01	0.09	2.91	4.52	0.17	0.09	0.05	0.02	0.40	6.41	84.14
	HD120104	3.9	61.90	23.07	0.02	0.15	2.96	5.17	0.21	0.07	0.02	0.02	0.48	6.02	80.29
	HD120105	4.9	59.47	24.21	0.07	0.16	3.49	5.35	0.24	0.07	0.10	0.02	0.57	6.29	79.94
	HD120106	5.9	60.87	23.73	0.01	1.40	2.65	4.89	1.20	0.16	0.11	0.02	0.43	5.79	81.20
	HD120107	6.9	61.75	22.75	0.01	0.10	3.05	5.93	0.23	0.12	0.16	0.03	0.48	5.30	77.22
	HD120108	7.9	65.06	21.27	0.01	0.08	2.36	4.92	0.21	0.12	0.11	0.03	0.38	5.38	79.33
S-facing mid-slope	HD113021	0.7	57.17	27.88	0.02	0.08	3.82	2.23	0.40	0.12	0.02	0.04	0.62	7.65	91.84
	HD113022	1.9	55.75	28.68	0.02	0.19	4.04	3.12	0.34	0.18	0.02	0.03	0.61	7.14	89.28
	HD113023	2.9	55.90	29.02	0.01	0.10	3.71	2.92	0.33	0.12	0.02	0.05	0.60	7.29	90.02
	HD113024	3.9	57.55	26.69	0.02	0.10	3.78	3.14	0.49	0.09	0.20	0.06	0.55	7.30	87.64
	HD113025	4.9	57.15	26.62	0.01	0.95	3.60	3.47	0.93	0.15	0.15	0.05	0.55	7.17	86.86
	HD113026	5.9	55.19	28.23	0.02	0.57	3.88	3.97	0.50	0.17	0.22	0.04	0.58	7.08	85.77
	HD113027	6.9	53.76	28.18	0.03	0.08	3.94	5.10	0.33	0.20	0.56	0.08	0.55	6.95	81.27
	HD113028	7.9	56.14	27.31	0.02	0.13	3.75	4.76	0.44	0.13	0.08	0.07	0.55	6.50	83.70
N-facing mid-slope	HD112906	0.4	50.78	31.79	0.02	0.09	5.04	1.83	0.53	0.10	0.02	0.04	0.64	9.15	93.97
	HD112907	1.5	57.11	27.39	0.01	0.15	3.83	1.71	0.36	0.08	0.05	0.03	0.58	8.82	93.36
	HD112908	2.9	55.05	28.46	0.02	0.10	4.24	3.14	0.38	0.16	0.10	0.09	0.64	7.61	88.76
	HD112909	4.3	59.08	24.86	0.02	0.10	3.39	3.53	0.43	0.14	0.02	0.09	0.55	7.76	86.50
	HD112910	5.4	59.79	24.31	0.02	0.49	3.63	4.06	0.31	0.21	0.06	0.06	0.56	6.79	84.28
	HD112911	6.5	61.60	22.93	0.03	0.17	3.42	4.23	0.49	0.12	0.03	0.10	0.55	6.28	83.01
	HD113002	7.6	56.59	26.86	0.02	0.11	3.70	4.77	0.58	0.16	0.07	0.06	0.62	6.35	83.45
	HD113003	8.5	54.88	26.69	0.02	0.07	4.00	5.67	1.16	0.20	0.06	0.06	0.65	6.28	80.97
Base	HD113013	0.6	45.61	34.40	0.04	0.23	5.92	1.67	0.55	0.04	0.11	0.07	0.73	10.82	94.33
	HD113014	1.8	53.30	29.88	0.01	0.12	4.19	3.40	0.39	0.10	0.01	0.04	0.66	7.85	88.99
	HD113015	2.8	56.33	27.58	0.02	0.13	3.68	4.70	0.27	0.11	0.02	0.02	0.62	6.55	84.28
	HD113016	3.9	58.00	25.94	0.02	0.14	3.43	4.84	0.26	0.14	0.05	0.04	0.53	6.48	82.88
	HD113017	4.9	59.70	23.79	0.01	0.19	3.47	5.02	0.80	0.12	0.19	0.03	0.56	6.08	80.48
	HD113018	5.9	56.58	27.02	0.02	0.15	3.64	5.36	0.28	0.12	0.06	0.04	0.59	5.99	81.97
	HD113019	7.0	59.31	24.66	0.01	0.10	3.44	5.43	0.28	0.14	0.03	0.04	0.51	5.85	80.59
	HD113020	8.1	60.65	23.38	0.03	0.10	3.21	5.51	0.47	0.13	0.13	0.05	0.50	5.59	78.97
Bedrock	HDZK05	32.0	65.10	16.06	2.38	1.35	3.09	4.99	0.77	0.08	3.78	0.17	0.57	2.74	50.17

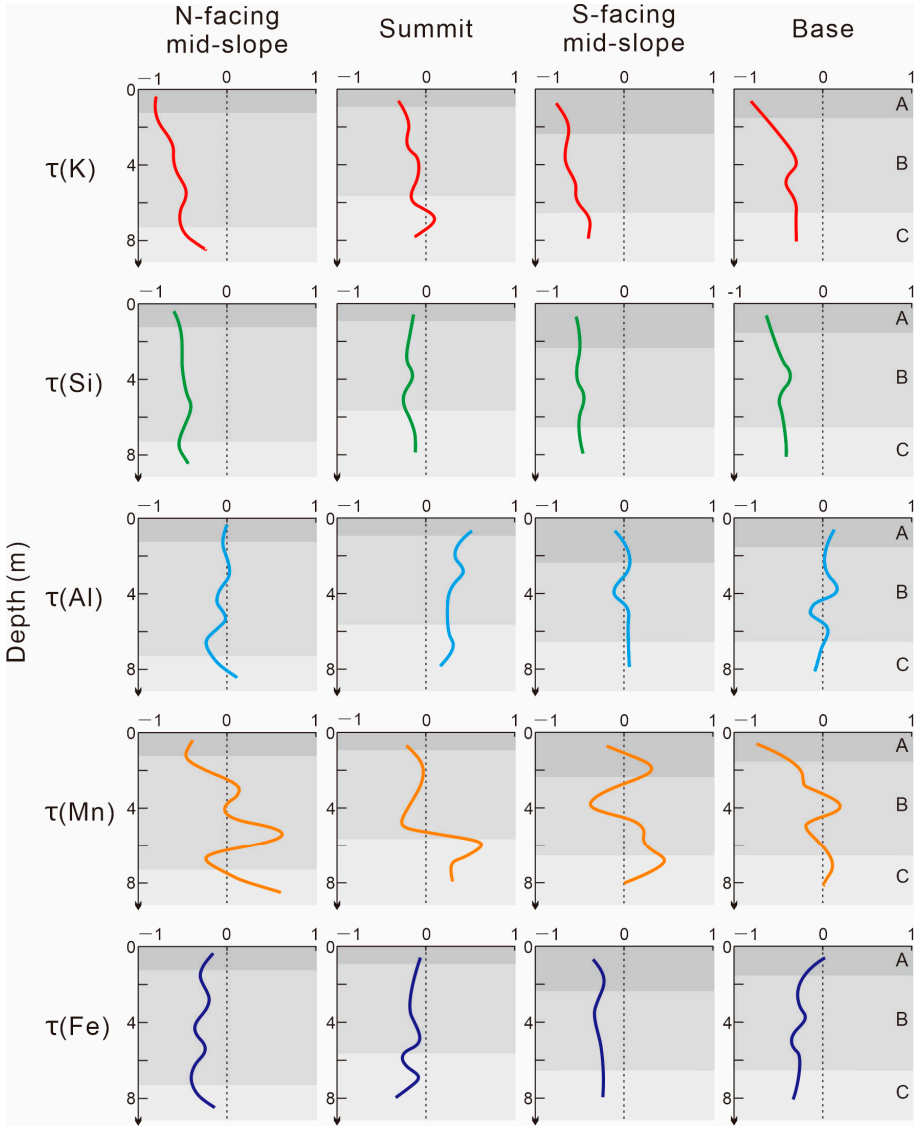

Figure 7. Plots of major elements' mass transfer coefficient versus depth for the studied weathering profiles. A—humus and clay horizon; B—fully weathered horizon; C—semi-weathered horizon.

The chemical index of alteration (CIA) was used to quantify the degree of chemical weathering. CIA = $Al_2O_3/(Al_2O_3 + CaO^* + Na_2O + K_2O) \times 100$, where the oxides represent molar quantities, and CaO* refers to CaO only in silicates, using McLennan's method for correction [27]. All the profiles have high CIA values (>85%) in A horizons, which decrease progressively from the surface to greater depths (Figure 8). The sequence of average CIA values is as follows: mid-slope (87) > base (84) > summit (81). From Table 3 and Figure 8, it can be observed that in the S-facing mid-slope profile, the CIA values of both the A and B horizons are greater than 85%, while in the N-facing mid-slope profile, the CIA values of the A horizon and most of the B horizon are also greater than 85%. The layers with CIA values greater than 85% can reach a depth of 5 m in these two mid-slope profiles. However, in the summit profile, only the A horizon above 1 m has CIA values greater than 85%. The conditions observed in the base profile are intermediate between those of the mid-slope and summit profiles. This trend correlates with variations in the total thickness of the A and B horizons, mineral abundances, and the loss and enrichment of major elements within the weathering profiles. The intensity of chemical weathering is greatest at the mid-slope and least at the summit.

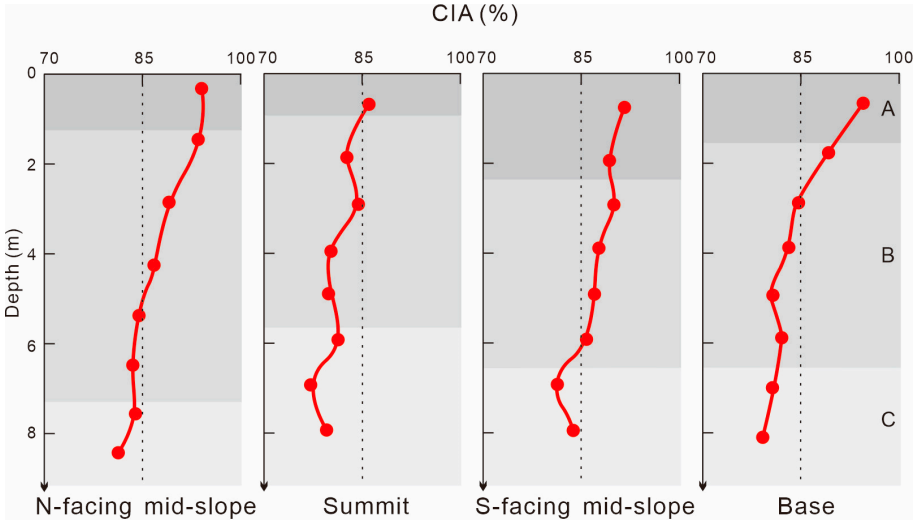

Figure 8. Plots of CIA values versus depth for the studied weathering profiles. A—humus and clay horizon; B—fully weathered horizon; C—semi-weathered horizon.

5.4. REE Compositions

The REE data are presented in Table 4, and chondrite-normalized REE patterns are presented in Figure 9. The chondrite data are sourced from C1 chondrite [28]. The REE contents are plotted versus depth in Figure 9. The parent rock has a total REE content of 235 ppm, with a total light REE (LREE) content of 200 ppm, which is much higher than the total HREE content of 35 ppm, resulting in an LREE/HREE ratio of 5.7. This characteristic is apparent for all four weathering profiles, which are LREE-dominated based on the chondrite-normalized REE patterns (Figure 9). However, the profiles exhibit varying degrees of REE enrichment, with contents of 247–1111 ppm at the mid-slope, 256–728 ppm at the summit, and 255–544 ppm at the base. In the four profiles (Figure 10), the REEs are predominantly enriched in the B horizon, exhibiting either convex or concave patterns with depth. At the mid-slope, the REEs are mainly concentrated in the middle of the B horizon. At the base, the enrichment is shallower and located primarily in the upper B horizon. At the summit, the enrichment is deeper, and mainly concentrated near the interface between the B and C horizons. The LREE/HREE values of the profiles are 1.6–20.5, with an average of 6.3 (n = 32), which is slightly higher than that of the parent rock. The accumulation depth of the HREEs is lower as compared with the LREEs, and the degree of REE fractionation is more pronounced at the N-facing mid-slope as compared with the S-facing mid-slope.

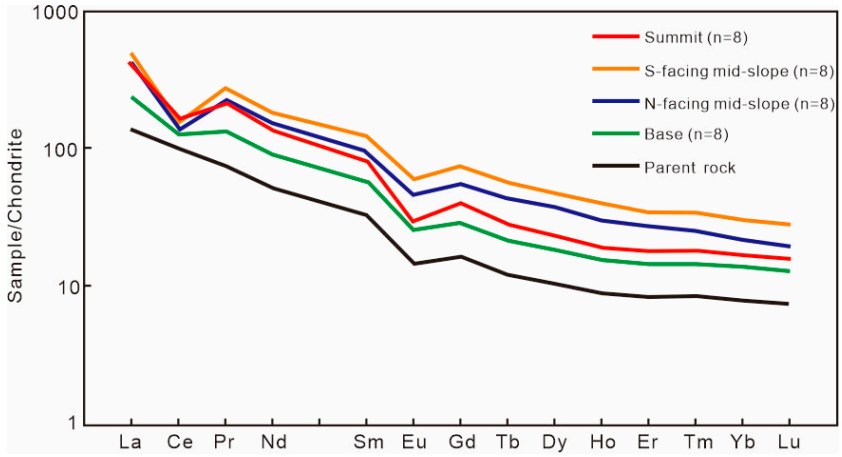

Figure 9. Chondrite-normalized REE patterns of the weathering profiles and parent rock.

Table 4. REE concentrations measured by ICP-MS for the studied weathering profiles and parent rock.

Profile Location	Sample Number	Depth (m)	REE Content (ppm)															REE (ppm)	LREE /HREE
			La	Ce	Pr	Nd	Sm	Eu	Gd	Tb	Dy	Ho	Er	Tm	Yb	Lu	Y		
Summit	HD120101	0.6	41	149	9	31	6	1	3	0	2	0	1	0	1	0	10	256	12.7
	HD120102	1.8	151	129	32	100	18	2	10	1	6	1	3	0	3	0	27	484	8.4
	HD120103	2.9	203	188	40	130	24	3	15	2	9	2	5	1	4	1	45	672	7.1
	HD120104	3.9	189	93	37	115	23	3	15	2	11	2	5	1	5	1	51	552	5.0
	HD120105	4.9	214	113	40	134	26	4	18	3	14	3	7	1	6	1	70	653	4.3
	HD120106	5.9	171	283	32	107	22	3	16	2	13	2	6	1	6	1	64	728	5.6
	HD120107	6.9	142	114	27	90	18	2	12	2	10	2	5	1	5	1	52	481	4.4
	HD120108	7.9	120	153	23	77	15	2	10	1	8	1	4	1	4	1	39	458	5.7
S-facing mid-slope	HD113021	0.7	105	209	24	78	15	2	7	1	5	1	3	0	3	0	20	473	10.7
	HD113022	1.9	188	213	44	154	30	4	15	2	8	2	4	1	4	1	37	706	8.7
	HD113023	2.9	205	97	46	151	30	5	17	2	10	2	5	1	5	1	45	621	6.1
	HD113024	3.9	232	102	48	177	37	7	26	3	17	3	9	1	8	1	84	755	4.0
	HD113025	4.9	252	199	50	178	40	8	34	5	27	5	13	2	11	1	137	963	3.1
	HD113026	5.9	252	121	48	168	43	9	41	6	36	7	17	2	14	2	188	955	2.0
	HD113027	6.9	170	135	32	112	29	6	31	5	31	6	14	2	12	2	173	758	1.8
	HD113028	7.9	86	106	16	57	13	3	13	2	14	3	7	1	6	1	82	408	2.2
N-facing mid-slope	HD112906	0.4	30	208	5	19	4	1	2	0	2	0	1	0	2	0	10	285	14.7
	HD112907	1.5	55	118	12	34	5	1	3	0	2	0	1	0	2	0	11	247	10.9
	HD112908	2.9	243	99	54	192	30	4	13	1	6	1	3	0	3	0	24	675	11.8
	HD112909	4.3	367	115	71	249	50	9	33	4	19	3	9	1	7	1	83	1021	5.4
	HD112910	5.4	288	174	51	186	49	10	48	8	43	8	19	3	15	2	209	1111	2.1
	HD112911	6.5	160	88	28	97	25	5	28	5	30	5	14	2	10	1	159	659	1.6
	HD113002	7.6	60	81	11	40	8	2	7	1	6	1	3	0	3	0	35	259	3.6
	HD113003	8.5	53	114	11	39	8	1	5	1	4	1	2	0	2	0	23	267	5.7
Base	HD113013	0.6	37	268	6	18	4	1	3	0	2	0	1	0	1	0	9	350	20.5
	HD113014	1.8	93	131	21	77	13	2	8	1	5	1	3	0	3	0	24	383	7.5
	HD113015	2.8	149	108	34	125	23	4	16	2	11	2	6	1	5	1	56	544	4.4
	HD113016	3.9	132	54	28	101	22	4	16	2	14	3	7	1	6	1	72	463	2.8
	HD113017	4.9	97	142	20	70	15	3	11	2	9	2	5	1	4	1	50	430	4.1
	HD113018	5.9	77	99	16	55	12	2	8	1	6	1	3	0	3	0	32	317	4.7
	HD113019	7.0	60	90	12	43	9	2	6	1	5	1	3	0	2	0	24	257	5.2
	HD113020	8.1	54	108	11	38	8	1	5	1	4	1	2	0	2	0	20	255	6.3
Bedrock	HDZK05	32.0	50	95	10	36	8	1	5	1	4	1	2	0	2	0	20	235	5.7

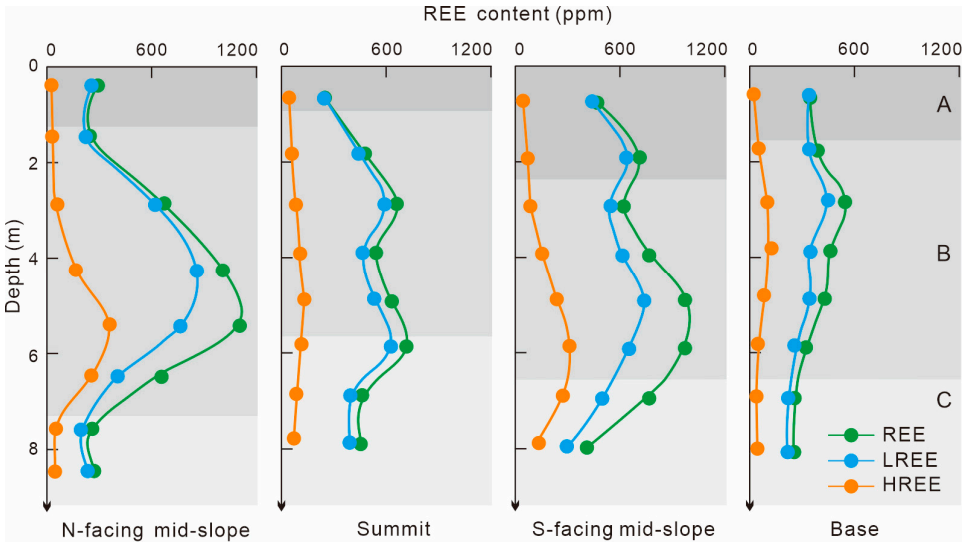

Figure 10. Plots of REE content versus depth for the studied weathering profiles. A—humus and clay horizon; B—fully weathered horizon; C—semi-weathered horizon.

6. Discussion

6.1. Comparison of Weathering Degrees Along the Hillslope

The mineral composition of all profiles on the knoll is relatively simple, characterized by high quartz content, low concentrations of alkali feldspar, and kaolinite as the dominant clay mineral, indicating an intense degree of weathering [29,30]. Primary minerals prone to weathering, such as plagioclase, biotite, amphibole, and apatite, are largely absent from the profiles. In comparison, the mid-slope exhibits lower alkali feldspar concentrations and higher clay content, distinguishing it from both the summit and base, suggesting that it has undergone more pronounced chemical weathering. The absence of gibbsite at the summit indicates its relatively low weathering degree. The complete depletion of active Na and Ca and the enrichment of inert Al elements indicate that weathering has advanced to a significant stage. At the summit, the depletion of K and Si is less pronounced than in other profiles, while Al is distinctly enriched at the summit but remains unchanged in the other profiles, indicating a relatively lower weathering intensity. The CIA provides a clearer metric for assessing chemical weathering [27], with results indicating mid-slope > base > summit. The quantitative results provide robust support for the preceding analyses of mineral composition and major element concentrations.

6.2. REE Enrichment and Leaching

The relationship between REE content and chemical weathering intensity (Figure 11a) shows that for 65% < CIA < 85%, REE contents positively correlate with CIA values. In this range, mildly acidic precipitation and soil humus contribute to the release of REEs from bedrock, enabling them to migrate as free ions or complexes [31–33]. Ion exchange facilitates REE adsorption onto secondary clay minerals, leading to REE enrichment [13,34,35].

Conversely, when the CIA exceeds 85%, the REE content shows a negative correlation with CIA (Figure 11a). In profiles, clay mineral concentration increases from bottom to top; however, REE content does not follow this trend. Researchers note that secondary clay minerals evolve from diverse types to a more homogeneous form as weathering progresses, shifting from a 2:1 type with higher REE adsorption capacity to a less effective 1:1 type [15,20]. In the upper layers, the evolution of clay minerals combined with intensified water leaching and changes in physicochemical conditions (e.g., increased acidity) makes REE adsorption less favorable [5,36,37].

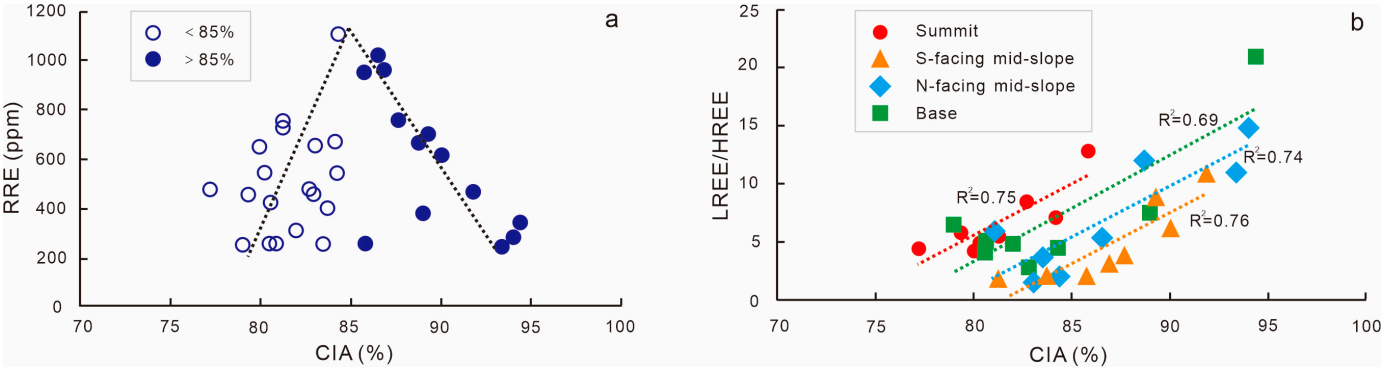

Figure 11. Plots of (**a**) REE contents and (**b**) LREE/HREE versus CIA values for the studied weathering profiles.

In the mid-slope, intensified weathering releases sufficient ionic REEs and increases clay mineral content, which boosts REE adsorption, especially due to illite's superior adsorption efficiency compared to kaolinite [38,39]. This combination contributes to greater REE enrichment across the knoll's mid-slope. However, at the summit, weathering is weaker, yet REE content and enriched layer thickness are higher than at the base, likely due to the strong leaching effects of the base (discussed in Section 6.4).

6.3. REE Fractionation and Anomaly of Ce and Eu

Due to the distinct physicochemical characteristics of LREEs and HREEs, including their redox behavior and hydrolysis constants, weathering processes preferentially leach HREEs over LREEs, resulting in REE fractionation [40–42]. In the profiles of the knoll, the LREE/HREE ratios increase in correlation with CIA values (Figure 11b), reflecting that enhanced chemical weathering leads to significant LREE/HREE fractionation [43–45].

For a given CIA value, the order of LREE/HREE ratios in profiles is as follows: summit > base > mid-slope, with N-facing mid-slope > S-facing mid-slope (Figure 11b). This reflects the hierarchical degree of REE fractionation. It is essential to recognize that clay minerals also play a significant role in REE fractionation; the abundance of these minerals and the presence of illite enable the retention of more HREEs with minimal desorption. This could explain the lower degree of REE fractionation on mid-slopes.

Ce and Eu are sensitive to redox processes, and their anomalies reflect the degree of separation from other REEs and are widely used to assess redox conditions during weathering [46]. $\delta Ce = Ce_N/((La_N \times Pr_N)1/2)$ and $\delta Eu = Eu_N/((Sm_N \times Gd_N)1/2)$, where N represents normalization by C1 chondrite [28]. The δCe curve exhibits a "C" shape, with Ce showing a positive anomaly in the A horizon of all profiles that gradually transitions to a stable negative anomaly at greater depths. In contrast, δEu displays a distinct negative anomaly (Figure 12). In the A horizon, Ce^{3+} oxidizes to Ce^{4+}, forming CeO_2 precipitates and resulting in a positive anomaly, while Eu shows a negative anomaly inherited from the bedrock. Simultaneously, the Fe^{3+}/Fe^{2+} ratio is utilized for verification, indicating that oxidation intensifies from the bottom of the B horizon upwards to the A horizon, aligning with δCe results (Figure 12).

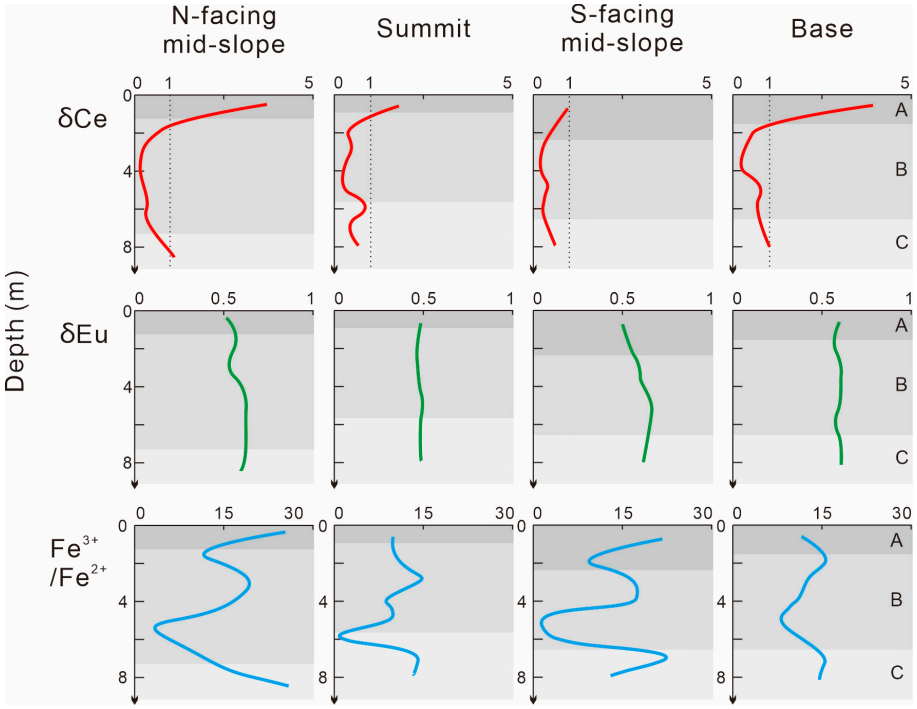

Figure 12. Plots of δCe, δEu, and Fe^{3+}/Fe^{2+} versus depth for the studied weathering profiles. A—humus and clay horizon; B—fully weathered horizon; C—semi-weathered horizon.

6.4. Illuviation Effects on REE Distribution

In the preceding discussion, it is clear that the redistribution of REEs on the knoll is linked to illuviation effects. While the water content across the four profiles represents a transient condition within the context of prolonged weathering processes, it nonetheless provides a robust foundation for a further analysis. In granite regions characterized by a uniform lithology and minimal tectonism, the redistribution of water within the weathering profile of a knoll is affected mainly by the topography [47–49]. Under the influence of topography, the direction and intensity of water infiltration and leaching, coupled with chemical weathering, collectively determine the depth and extent of secondary REE enrichment horizons on the knoll (Figure 13a).

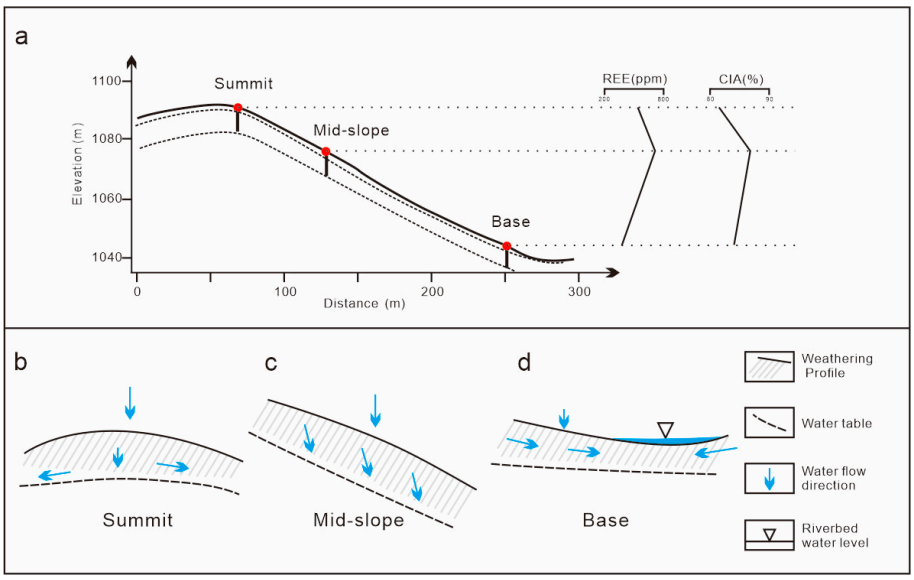

Figure 13. (**a**) Comparison of REE contents and CIA value and (**b**–**d**) water flow directions on knoll.

At the summit, water enters the weathering profile and flows divergently, with significant lateral divergence allowing for effective drainage (Figure 13b). Due to weaker chemical weathering, the A_2 and B horizons are thin, leading to minor REE release from primary minerals. Some REEs are lost laterally with the water flow [20], resulting in modest enrichment at the interface between the B and C horizons. At the mid-slope, vertical leaching is more prominent (Figure 13c). With advanced chemical weathering and a high clay mineral content, significant REEs are released and adsorbed, enriching in the middle B horizon [50,51]. At the base, the area is a runoff zone with abundant lateral water flow (Figure 13d). Although chemical weathering is more intense here compared to the summit, high lateral flow can carry REEs away, resulting in only minor REE enrichment in the upper B horizon.

Topographically controlled hydrological processes significantly affect LREE/HREE fractionation. The HREEs are more susceptible to transport by water infiltration and leaching compared to LREEs. At the summit, water flow is divergent, and at the base, lateral water flow is abundant. In both profiles, HREEs experience greater leaching. This dynamic leads to stronger REE fractionation at the summit and the base compared to the mid-slope. Discrepancies in REE fractionation between the N-facing and S-facing midslopes are noted. The slope aspect influences solar radiation levels, leading to varying temperature and moisture conditions. Due to the higher water content and greater thickness of the A and B horizons, the N-facing mid-slope profile experiences reduced evaporation and a stronger vertical leaching process. The N-facing mid-slope leaches more HREEs, likely due to this enhanced leaching process, thereby yielding a higher LREE/HREE ratio compared to the S-facing mid-slope [52–55].

On the knoll, the REE distribution varies significantly in different topographic settings. Topography controls the hydrological conditions, with water flow serving as both an external agent and a medium for REE migration. This makes water flow a key factor in controlling the geochemical behavior of the REEs [20,56–59]. Along with factors such as the parent rock, climate, and vegetation, the topography affects the activation, migration, fractionation, and enrichment of REEs [6,8,24,60–62]. These combined effects promote the development of ion-adsorption REE deposits. Gaining a deeper understanding of how micro-topographic factors affect the REEs in weathering profiles is important for the exploration, resource estimation, and efficient utilization of ion-adsorption REE deposits.

7. Conclusions

This study investigated the mineralogical and geochemical characteristics of weathering profiles developed at various topographic positions on a knoll within the Hedi ion-adsorption REE deposit in Zhejiang Province, China. The main conclusions are as follows.

1. The weathering profiles are layered. The mid-slope features the thickest and best-developed A_2 and B horizons, followed by the base and then summit. The thickness, mineral composition, and major element characteristics of these horizons correlate with the CIA. The order of the CIA values is mid-slope > base > summit. This suggests that the highest intensity of chemical weathering is at the mid-slope and the lowest intensity is at the summit.
2. The REEs are most concentrated in the B horizon, with the greatest enrichment at the mid-slope, followed by the summit and then base. The depths of enrichment are in the order summit > mid-slope > base. The REE fractionation in the regolith is more pronounced than in the parent rock, with the HREEs being concentrated at greater depths as compared with the LREEs. In addition, REE fractionation is stronger on the N-facing mid-slope as compared with the S-facing mid-slope.
3. The enrichment and fractionation of REEs are closely linked to the chemical weathering intensity and clay minerals. During weathering, REE contents initially increase before decreasing. The intensified weathering and higher clay mineral content combined with the presence of illite are reasons for higher REE concentration in mid-slopes. Chemical weathering enhances LREE/HREE fractionation. Clay minerals also play a

significant role in REE fractionation. The Ce anomaly result supports the viewpoint that oxidation conditions enhance upward in the profile.

4. Water leaching influenced by the micro-topography affects both the depth and extent of REE enrichment. Micro-topographic hydrological variations affect LREE/HREE fractionation. In addition, the slope orientation affects REE fractionation due to variations in temperature and moisture.

Author Contributions: Conceptualization, W.G.; Formal analysis, W.G.; Investigation, W.G., X.C. and C.Z.; Resources, X.C., X.D., W.Z. and C.Z.; Data curation, W.G.; Writing—original draft, W.G.; Writing—review and editing, W.G., Z.Z., C.W. and D.W.; Visualization, W.G.; Supervision, Z.Z.; Project administration, W.G. and Z.Z.; Funding acquisition, Z.Z. All authors have read and agreed to the published version of the manuscript.

Funding: This research was supported by the Project: Study on the Mineralization Mechanism of Certain REE Deposits in Jiangxi Province (HE2417).

Data Availability Statement: Data are contained within the article.

Acknowledgments: Thanks for the great effort by Wang Cheng-Hui, Zhao Zheng, Fan Xi-Yin, Yang Yue-Qing, Rao Jiao-Ping, and all reviewers.

Conflicts of Interest: The authors declare no conflicts of interest. The funders had no role in the design of the study; in the collection, analyses, or interpretation of data; in the writing of the manuscript; or in the decision to publish the results.

References

1. Goodenough, K.M.; Wall, F.; Merriman, D. The Rare Earth Elements: Demand, Global Resources, and Challenges for Resourcing Future Generations. *Nat. Resour. Res.* **2017**, *27*, 201–216. [CrossRef]
2. Wall, F.; Rollat, A.; Pell, R.S. Responsible Sourcing of Critical Metals. *Elements* **2017**, *13*, 313–318. [CrossRef]
3. Xu, C.; Kynický, J.; Smith, M.P.; Kopriva, A.; Brtnický, M.; Urubek, T.; Yang, Y.; Zhao, Z.; He, C.; Song, W. Origin of heavy rare earth mineralization in South China. *Nat. Commun.* **2017**, *8*, 14598. [CrossRef]
4. Li, Y.H.M.; Zhao, W.W.; Zhou, M.-F. Nature of parent rocks, mineralization styles and ore genesis of regolith-hosted REE deposits in South China: An integrated genetic model. *J. Asian Earth Sci.* **2017**, *148*, 65–95. [CrossRef]
5. Zhao, Z.; Wang, D.H.; Chen, Z.H.; Chen, Z.Y. Progress of Research on Metallogenic Regularity of Ion-adsorption Type REE Deposit in the Nanling Range. *Acta Geol. Sin.* **2017**, *91*, 2814–2827. (In Chinese)
6. Wu, C.Y. The Study of Ion-Adsorbed Type of Rare Earth Deposits in Weathering Crust from South Jiangxi and North Guangdong Provinces. Ph.D. Thesis, Graduate School of Chinese Academy of Geological Sciences, Beijing, China, 1988. (In Chinese)
7. Bai, G.; Wu, C.Y.; Ding, X.S.; Yuan, Z.X.; Huang, D.H.; Wang, P.H. *Genesis and Spatial Distribution of Ion-Adsorption Type REE Deposits in Nanling Region*; Institute of Ore Deposits Geology: Beijing, China, 1989. (In Chinese)
8. Chen, B.H.; Wang, Z.M.; Huang, L.M.; Wu, F.H.; Chen, J.D.; Xu, W.L. An Experimental Study on the Effects of Microbes on the Migration and Accumulation of REE in the Weathering Crust of Granite. *Chin. J. Geochem.* **2000**, *19*, 280–288. [CrossRef]
9. Moldoveanu, G.A.; Papangelakis, V.G. Recovery of rare earth elements adsorbed on clay minerals: I. Desorption mechanism. *Hydrometallurgy* **2012**, *117–118*, 71–78. [CrossRef]
10. Borst, A.M.; Smith, M.P.; Finch, A.A.; Estrade, G.; Villanova-de-Benavent, C.; Nason, P.; Marquis, E.; Horsburgh, N.J.; Goodenough, K.M.; Xu, C.; et al. Adsorption of rare earth elements in regolith-hosted clay deposits. *Nat. Commun.* **2020**, *11*, 4386. [CrossRef]
11. Wu, Z.X.; Chen, Y.; Wang, Y.; Xu, Y.; Lin, Z.L.; Liang, X.L.; Cheng, H.F. Review of rare earth element (REE) adsorption on and desorption from clay minerals: Application to formation and mining of ion-adsorption REE deposits. *Ore Geol. Rev.* **2023**, *157*, 105446. [CrossRef]
12. Zhang, Z.H. A study on weathering crust ion-adsorption type REE deposits, south China. *Contrib. Geol. Miner. Resour. Res.* **1990**, *5*, 57–71. (In Chinese)
13. Bao, Z.W.; Zhao, Z.H. Geochemistry of mineralization with exchangeable REY in the weathering crusts of granitic rocks in South China. *Ore Geol. Rev.* **2008**, *33*, 519–535. [CrossRef]
14. Zhao, Z.; Wang, D.H.; Chen, Z.Y.; Guo, N.X.; Liu, X.X.; He, H.H. Metallogenic specialization of rare earth mineralized igneous rocks in the Eastern Nanling Region. *Geotecton. Metallog.* **2014**, *38*, 255–263. (In Chinese)
15. Chi, R.A.; Tian, J.; Luo, X.P.; Xu, Z.G.; He, Z.Y. The basic research on the weathered crust elution-deposited rare earth ores. *Nonferrous Met. Sci. Eng.* **2012**, *3*, 1–13. (In Chinese)
16. Liu, X.X.; Chen, Y.C.; Wang, D.H.; Huang, F.; Zhao, Z. The Metallogenic Geomorphic Condition Analysis of the Ion-absorbing Type Rare Earths Ore in the Eastern Nanling Region Based on DEM Data. *Acta Geosci. Sin.* **2016**, *37*, 174–184. (In Chinese)
17. Wang, D.H.; Zhao, Z.; Yu, Y.; Zhao, T.; Li, J.K.; Dai, J.J.; Liu, X.X.; He, H.H. Progress, Problems and Research Orientation of Ion-adsorption Type Rare Earth Resources. *Rock Miner. Anal.* **2013**, *32*, 796–802. (In Chinese)

18. Fan, X.Y.; Zhang, A.P.; Guo, B.H. Geological Features of the Hedi Rare Earth Deposit in Qingyuan. In Proceedings of the Commemorating the 120th Anniversary of the Birth of Geologist Mr. Zhu Tinghu—2015 Annual Academic Conference of Zhejiang Geological Society, Hangzhou, China, 30 October 2015. (In Chinese)
19. Zhang, Z.Y.; Sun, N.J.; He, Z.Y.; Chi, R.A. Local concentration of middle and heavy rare earth elements in the col on the weathered crust elution-deposited rare earth ores. *J. Rare Earths* **2018**, *36*, 552–558. [CrossRef]
20. Li, M.Y.H.; Zhou, M.-F.; Williams-Jones, A.E. Controls on the Dynamics of Rare Earth Elements During Subtropical Hillslope Processes and Formation of Regolith-Hosted Deposits. *Econ. Geol.* **2020**, *115*, 1097–1118. [CrossRef]
21. Shi, Y.J.; Zhou, Q.M.; Shi, Q.; Li, X.L.; Wang, Y. Geochemical characteristics of HM ion-adsorption type REE deposit in Cenxi, Guangxi. In Proceedings of the Eleventh National Symposium on Exploration Geochemistry, Yinchuan, China, 23–26 July 2013. (In Chinese)
22. He, Y.; Cheng, L.; Li, Y.; Ran, D.J.; Wei, Q.S. The mineralization mechanism of the ion adsorption type rare earths ore and prospecting marks. *Chin. Rare Earths* **2015**, *36*, 98–103. (In Chinese)
23. Chen, C.; Wang, C.H.; Wang, D.H.; Qin, J.H.; Lu, L.; Dang, X.L.; Fan, X.Y.; Chen, X.R.; Zhang, W. U-Pb dating and Hf isotope characteristics of zircons from ore-forming parent rocks in the Qingyuan ion-adsorbed REE deposit, Zhejiang Province, China. *Acta Mineral. Sin.* **2020**, *40*, 58–72. (In Chinese)
24. Nesbitt, H.W. Mobility and fractionation of rare earth elements during weathering of a granodiorite. *Nature* **1979**, *279*, 206–210. [CrossRef]
25. Brimhall, G.H.; Dietrich, W.E. Constitutive mass balance relations between chemical composition, volume, density, porosity, and strain in metasomatic hydrochemical systems: Results on weathering and pedogenesis. *Geochim. Cosmochim. Acta* **1987**, *51*, 567–587. [CrossRef]
26. Anderson, S.P.; Dietrich, W.E.; Brimhall, G.H., Jr. Weathering profiles, mass-balance analysis, and rates of solute loss: Linkages between weathering and erosion in a small, steep catchment. *Geol. Soc. Am. Bull.* **2002**, *114*, 1143–1158. [CrossRef]
27. McLennan, S.M. Weathering and Global Denudation. *J. Geol.* **1993**, *101*, 295–303. [CrossRef]
28. Sun, S.S.; McDonough, W.F. Chemical and isotopic systematics of oceanic basalts: Implications for mantle composition and processes. *Geol. Soc. Lond. Spec. Publ.* **1989**, *42*, 313–345. [CrossRef]
29. Mikesell, L.R.; Schaetzl, R.J.; Velbel, M.A. Hornblende etching and quartz/feldspar ratios as weathering and soil development indicators in some Michigan soils. *Quat. Res.* **2017**, *62*, 162–171. [CrossRef]
30. Lee, M.R.; Hodson, M.E.; Brown, D.J.; MacKenzie, M.; Smith, C.L. The composition and crystallinity of the near-surface regions of weathered alkali feldspars. *Geochim. Cosmochim. Acta* **2008**, *72*, 4962–4975. [CrossRef]
31. Chen, D.Q.; Wu, J.S. Ore-forming mechanism of ion-adsorption type REE deposits. *J. Chin. Rare Earth Soc.* **1990**, *8*, 175–179. (In Chinese)
32. Aubert, D.; Stille, P.; Probst, A. REE fractionation during granite weathering and removal by waters and suspended loads: Sr and Nd isotopic evidence. *Geochim. Cosmochim. Acta* **2001**, *65*, 387–406. [CrossRef]
33. Zhou, M.-F.; Li, M.Y.H.; Wang, Z.C.; Li, X.C.; Liu, J.C. The genesis of regolith-hosted rare earth element and scandium deposits: Current understanding and outlook to future prospecting. *Chin. Sci. Bull.* **2020**, *65*, 3809–3824. (In Chinese) [CrossRef]
34. Chi, R.A.; Tian, J. Review of weathered crust rare earth ore. *J. Chin. Rare Earth Soc.* **2007**, *25*, 641–650. (In Chinese)
35. Kynicky, J.; Smith, M.P.; Xu, C. Diversity of Rare Earth Deposits: The Key Example of China. *Elements* **2012**, *8*, 361–367. [CrossRef]
36. Yang, T.; Gao, L.; Lu, Y.T. Rare earth elements characteristics and significance of Guangping granite weathering crust. *Chin. Rare Earths* **2018**, *39*, 32–40. (In Chinese)
37. Zhao, Z.; Wang, D.H.; Liu, X.X.; Zhang, Q.W.; Yao, M.; Gu, W.A. Geochemical features of rare earth elements in different weathering stage of the Guangxi Huashan granite and its influence factors. *Chin. Rare Earths* **2015**, *36*, 14–20. (In Chinese)
38. Yang, M.J.; Liang, X.L.; Ma, L.Y.; Huang, J.; He, H.P.; Zhu, J.X. Adsorption of REEs on kaolinite and halloysite: A link to the REE distribution on clays in the weathering crust of granite. *Chem. Geol.* **2019**, *525*, 210–217. [CrossRef]
39. Wainipee, W.; Cuadros, J.; Sephton, M.A.; Unsworth, C.; Gill, M.G.; Strekopytov, S.; Weiss, D.J. The effects of oil on As(V) adsorption on illite, kaolinite, montmorillonite and chlorite. *Geochim. Cosmochim. Acta* **2013**, *121*, 487–502. [CrossRef]
40. Chen, Y.; Wang, X.R.; Peng, A. The research progress of fractionation among the rare earth elements. *Adv. Environ. Sci.* **1999**, *7*, 10–17. (In Chinese)
41. Chi, R.A.; Xu, J.M.; He, P.J.; Zhu, Y.L. REE geochemistry of granitoid weathering crust and properties of ores in Southern China. *Geochimica* **1995**, *24*, 261–269. (In Chinese)
42. Chang, C.Y.; Li, F.B.; Liu, C.S.; Gao, J.F.; Tong, H.; Chen, M.J. Fractionation characteristics of rare earth elements (REEs) linked with secondary Fe, Mn, and Al minerals in soils. *Acta Geochim.* **2016**, *35*, 329–339. [CrossRef]
43. Middelburg, J.J.; Van der Weijden, C.H.; Woittiez, J.R.W. Chemical processes affecting the mobility of major, minor and trace elements during weathering of granitic rocks. *Chem. Geol.* **1988**, *68*, 253–273. [CrossRef]
44. Duzgoren-Aydin, N.S.; Aydin, A. Distribution of rare earth elements and oxyhydroxide phases within a weathered felsic igneous profile in Hong Kong. *J. Asian Earth Sci.* **2009**, *34*, 1–9. [CrossRef]
45. Yusoff, Z.M.; Ngwenya, B.T.; Parsons, I. Mobility and fractionation of REEs during deep weathering of geochemically contrasting granites in a tropical setting, Malaysia. *Chem. Geol.* **2013**, *349–350*, 71–86. [CrossRef]
46. Braun, J.J.; Pagel, M.; Muller, J.P.; Bilong, P.; Michard, A.; Guillet, B. Cerium anomalies in lateritic profiles. *Geochim. Gosmochimica* **1990**, *54*, 781–795. [CrossRef]

47. Liu, G.Y. *Bedrock Groundwater*; Geological Publishing House: Beijing, China, 1979; pp. 56–58. (In Chinese)
48. Detty, J.M.; McGuire, K.J. Topographic controls on shallow groundwater dynamics: Implications of hydrologic connectivity between hillslopes and riparian zones in a till mantled catchment. *Hydrol. Process.* **2010**, *24*, 2222–2236. [CrossRef]
49. Liu, J.T.; Han, X.L.; Liu, J.L.; Liang, Z.M.; He, R.M. Understanding of critical zone structures and hydrological connectivity: A review. *Adv. Water Sci.* **2019**, *30*, 112–122. (In Chinese)
50. Song, Z.; Wu, Y.; Yang, X.; Xu, Z.; Liu, L.; Zhang, X.; Hao, Q.; Sun, S.; Han, G.; Liu, C. Effects of topography and vegetation on distribution of rare earth elements in calcareous soils. *Acta Geochim.* **2017**, *36*, 469–473. [CrossRef]
51. Estrade, G.; Marquis, E.; Smith, M.; Goodenough, K.; Nason, P. REE concentration processes in ion adsorption deposits: Evidence from the Ambohimirahavavy alkaline complex in Madagascar. *Ore Geol. Rev.* **2019**, *112*, 103027. [CrossRef]
52. Lin, C.; Li, C.W. The significance of aspect in mountain geography. *Acta Geogr. Sin.* **1985**, *40*, 20–28. (In Chinese)
53. Carter, B.J.; Ciolkosz, E.J. Slope gradient and aspect effects on soils developed from sandstone in Pennsylvania. *Geoderma* **1991**, *49*, 199–213. [CrossRef]
54. Egli, M.; Mirabella, A.; Sartori, G.; Giaccai, D.; Zanelli, R.; Plötze, M. Effect of slope aspect on transformation of clay minerals in Alpine soils. *Clay Miner.* **2007**, *42*, 373–398. [CrossRef]
55. Li, M.; Yao, W.Y.; Li, Z.B.; Liu, P.L.; Shen, Z.Z. Effects of landforms on the erosion rate in a small watershed by the ^{137}Cs tracing method. *J. Environ. Radioact.* **2010**, *101*, 380–384. [CrossRef]
56. Yoo, K.; Amundson, R.; Heimsath, A.M.; Dietrich, W.E.; Brimhall, G.H. Integration of geochemical mass balance with sediment transport to calculate rates of soil chemical weathering and transport on hillslopes. *J. Geophys. Res.* **2007**, *112*, F02013. [CrossRef]
57. Yuan, Y.Y.; Liu, S.L.; Wu, M.; Zhong, M.Y.; Shahid, M.Z.; Liu, Y.L. Effects of topography and soil properties on the distribution and fractionation of REEs in topsoil: A case study in Sichuan Basin, China. *Sci. Total Environ.* **2021**, *791*, 148404. [CrossRef]
58. Liu, W.; Li, Y.; Wang, X.; Cui, L.; Zhao, Z.; Liu, C.; Xu, Z. Weathering stage and topographic control on rare earth element (REE) behavior: New constraints from a deeply weathered granite hill. *Chem. Geol.* **2022**, *610*, 121066. [CrossRef]
59. Luo, K.; Ma, J.L. Recent advances in migration and enrichment of rare earth elements during chemical weathering of granite. *Adv. Earth Sci.* **2022**, *37*, 692–708. (In Chinese)
60. Chen, Z.C.; Zhuang, W.M.; Yu, S.Y. Some new knowledge of REE migration and concentration mechanism in weathering crust of granites, South China. *Adv. Earth Sci.* **1993**, *8*, 47–48. (In Chinese)
61. Wang, D.H.; Zhao, Z.; Yu, Y.; Wang, C.H.; Dai, J.J.; Sun, Y.; Zhao, T.; Li, J.K.; Huang, F.; Chen, Z.Y.; et al. A review of the achievements in the survey and study of ion-adsorption type REE deposits in China. *Acta Geosci. Sin.* **2017**, *38*, 317–325. (In Chinese)
62. He, Y.L.; Ma, L.Y.; Li, X.R.; Wang, H.; Liang, X.L.; Zhu, J.X.; He, H.P. Mobilization and fractionation of rare earth elements during experimental bio-weathering of granites. *Geochim. Cosmochim. Acta* **2023**, *343*, 384–395. [CrossRef]